High-fidelity aerodynamic loads analysis of the double-swept ERATO rotor

Mikel Balmaseda, Hyeonsoo Yeo, Buvana Jayaraman, Biel Ortun

HIGH-FIDELITY AERODYNAMIC LOADS ANALYSIS OF THE DOUBLE-SWEPT ERATO ROTOR

Mikel Balmaseda Aguirre
DAAA/ONERA
Institut Polytechnique de Paris
Meudon, France

Hyeonsoo Yeo
U.S. Army Combat Capabilities Development
Command Aviation & Missile Center
Ames Research Center, Moffet Field, CA, USA

François Richez
DAAA/ONERA
Institut Polytechnique de Paris
Meudon, France

Buvana Jayaraman
U.S. Army Combat Capabilities Development
Command Aviation & Missile Center
Ames Research Center, Moffet Field, CA, USA

Biel Ortun
DAAA/ONERA
Institut Polytechnique de Paris
Meudon, France

ABSTRACT

In the literature was proven the validity of using comprehensive analysis (CA) tools coupled with computational fluid dynamics (CFD) to predict the aerodynamics of classical rotor blades. This paper aims to enhance this validation for the complex double-swept planform ERATO blade under high-advance-ratio level-flight condition. In order to do so, RCAS and HOST comprehensive analysis tools and Helios/RCAS and elsA/HOST high-fidelity loose couplings are compared to the results of the experimental campaign of the ERATO blade that was carried out by ONERA in 1998. Trim commands, airloads and pressure coefficient distribution on the chordwise direction are used to validate the numerical simulations. The results highlight the need for high-fidelity methods in order to accurately predict the aerodynamic response. The numerical data provided by the high-fidelity methods are used to analyse the flow features that are at the origin of the airloads variations, especially an interesting phenomenon is observed on the retreating blade where a pitching-moment dynamic stall without lift stall is induced by a leading edge vortex.

NOTATION

*

Symbols

A rotor disk area, πR^2

a speed of sound, m/s

c chord, m

C_L rotor lift coefficient, $L/\rho(\Omega R^2)A$

C_p pressure coefficient

C_X rotor propulsive force coefficient, $X/\rho(\Omega R^2)A$

f_m blade section pitching moment per unit length, N/m

f_n blade section normal force moment per unit length, N/m

L rotor lift, N

M^2C_m blade section pitching moment coefficient times Mach number squared, $f_m/\frac{1}{2}\rho a^2 c^2$

M^2C_n blade section normal force moment coefficient times Mach number squared, $f_n/\frac{1}{2}\rho a^2 c$

P power of the rotor, kW

R blade radius, m

r/R relative span

X rotor propulsive force, N

x/c normalised chord-wise coordinate

α_s shaft angle (positive for rearward tilt), deg

β_{1c}, β_{1s} longitudinal and lateral flappling, deg

θ_0 collective, deg

θ_{1c}, θ_{1s} lateral and longitudinal cyclic, deg

μ advance ratio

ρ freestream density, kg/m^3

σ rotor solidity

Ω rotor angular velocity, rad/s

INTRODUCTION

Over the last decades, aero-elastic simulations of helicopter rotor using high-fidelity methods based on CFD (Computational Fluid Dynamics) were developed and implemented. The improvement of this numerical approach was possible thanks to the growth of the computational resources that were essential to accurately capture the complex aerodynamic phenomena encountered around helicopter rotors. Based on high quality data of flight and wind-tunnel tests, the numerical simulations have been successfully validated for the full-scale UH-60A rotor (Refs. 1–3) and the model-scale 7A and 7AD rotors in forward flight (Refs. 4–7). These publications showed that airloads and structural loads can be predicted with satisfactory agreement. However, for nonclassical blade-shapes like the double-swept ERATO blade (Étude d'un Rotor Aéroacoustique Technologiquement Optimisé) the existing literature is reduced (Refs. 8, 9). In 1998 the ERATO blade was tested at S1MA transonic wind tunnel at ONERA's Modane-Avrieux center as shown in Figure 1. Despite the long-date experiments of the ERATO rotor, no validation of the existing aeromechanical tools were performed previously (Ref. 10).

The high-velocity and the high-advance-ratio flight conditions were largely studied in the past years with the development of the Racer by Airbus Helicopters high-speed compound helicopter demonstrator (Refs. 11–13) and the Raider co-axial rotor helicopter by Sikorsky (Ref. 14).

In the framework of the United States/France Project Agreement on Rotatory Wing Aeromechanics and Human Factors Integration Research, the U.S. Army Combat Capabilities Development Command Aviation & Missile Center (DEVCOM AvMC) and ONERA, The French Aerospace Lab, have conducted research to investigate the airloads and structural loads of the ERATO rotor. The objective is to assess the accuracy of the prediction the ERATO rotor blade loads for various operating points.

This work is focused on the aerodynamic analysis of the ERATO rotor using high-fidelity coupled CFD/CA (comprehensive analysis) and standalone comprehensive analysis (CA) tools for the high-advance-ratio operating point. A companion paper (Ref. 15) by the same authors of the present paper examines the structural loads.

Figure 1: ERATO setup in ONERA's S1MA wind tunnel.

METHODS

The analytical results were obtained using both standalone comprehensive analyses and coupled CFD/CA analyses. ONERA used elsA (Ref. 16) for CFD and HOST (Ref. 17) for CA, and the U.S. Army used Helios (Ref. 18) for CFD and RCAS (Refs. 19, 20) for CA. Descriptions of each analysis and how they are coupled to produce a higher fidelity solution are provided in this section.

elsA

The elsA CFD code (Ref. 16), developed at ONERA, solves the unsteady Reynolds-Averaged Navier-Stokes (URANS) equations for both background Cartesian grids and blade curvilinear grids. Cartesian grid generation and overset grid assembly is done automatically by the pre- and post-processing tool Cassiopee (Ref. 21). The spatial discretization of the equations is performed with Jameson's cell-centered second order scheme, using 2nd and 4th order coefficients of artificial viscosity. The unsteady algorithm corresponds to a backward Euler scheme, with an implicit Gear scheme for the 2nd-order time integration. The time step is equivalent to 0.25 deg of blade rotation. The non-linear problem is solved iteratively with 30 Newton sub-iterations. Turbulence is taken into account by the Kok $k-\omega$ (Ref. 22) model, with Menter shear stress transport (SST) corrections (Ref. 23) and Zheng limiter (Ref. 24). The flow is modeled as fully turbulent. The near-body grids of the blades are rotated and deformed following the blade motion and trim provided, through the loose partitioned coupling, by the rotorcraft comprehensive analysis HOST.

HOST

HOST (Helicopter Overall Simulation Tool) (Ref. 17) is a rotorcraft comprehensive analysis developed by Airbus Helicopters. HOST modeling of blade dynamics is multibody-like. The blade is represented as an assembly of rigid segments connected by virtual joints. Euler-beam modeling provides 3 degrees of freedom (flapwise bending, chordwise bending, and torsion). A modal reduction approach is used to reduce the number of degrees of freedom from a large system of equations. The aerodynamics of HOST uses a lifting line approach based on airfoil look-up tables combined with a wake model. In this effort, among the several wake models available, a prescribed wake helical geometry was used. For the coupling with elsA, HOST airloads are corrected, via the delta method (Ref. 1), by the CFD airloads.

The ERATO rotor blade is modeled in HOST using 34 rigid elements connected by virtual hinges (flap, lag, and tor- sion). Blade dynamic responses are calculated with eight modes and eight harmonics. Section lift, drag, and moment values for the airfoils are obtained from airfoil look-up tables. Due to proprietary issues, the original airfoil tables used by ONERA were not shared with the U.S. Army. Thus, the airfoil tables are calculated from C81Gen by the U.S. Army. C81Gen is a Navier-Stokes based program that generates an airfoil table in C81 format. C81Gen runs two-dimensional, time-dependent compressible solver ARC2D with structured body fitted viscous gridding. ONERA performed HOST analysis with the two sets of airfoil tables and confirmed that rotor performance and loads agree reasonably well. For the current study, both HOST and RCAS used the C81Gen generated airfoil tables. A 5.0 deg azimuthal step size was used for the structural dynamics and trim calculations in HOST.

Helios

Helios (HELIcopter Overset Simulations) (Ref. 18), developed by the U.S. Army and the Department of Defense Computational Research and Engineering Acquisition Tools and Environments - Air Vehicles (CREATE^{TM}-AV) program, is a multidisciplinary computational platform for high-fidelity rotorcraft analysis. Helios uses a multi-mesh, multi-solver paradigm. Near-body solvers such as NASA's OVERFLOW (Ref. 25) structured solver and FUN3D (Ref. 26) unstructured solver, kCFD unstructured solver (Ref. 27), and mStrand multi-strand solver (Ref. 28) are integrated in Helios to capture the wall-bounded viscous effects. Cartesian grids in the off-body are used to resolve the wake through a combination of higher-order algorithms and adaptive mesh refinement (AMR). The Cartesian off-body grids are solved with SAMCart using a 5th-order central difference scheme in space and either a 3rd-order explicit 3-stage Runge-Kutta scheme or 2nd-order implicit lower-upper symmetric-Gauss- Seidel method (LU-SGS) BDF2 in time. An overset procedure facilitates data exchange and also enables relative motion between meshes using the parallel domain connectivity solver PUNDIT (Parallel UNsteady Domain Information Transfer). Helios also has the ability to perform CFD/CA coupling using the comprehensive analysis codes RCAS and CAMRAD II (Ref. 29) which allows the blades to be trimmed throughout the course of these simulations.

In this effort Helios solves the near-body grids around the rotor blades and test stand with the CFD solver OVERFLOW, using a 5th-order central difference scheme in space and a 2nd-order backward differentiation formula (BDF2) scheme in time. The fully turbulent flow is modeled using the Spalart-Allmaras delayed detached eddy simulation (DDES) turbulence model in both the near- and off-body grids. The time step is equivalent to an azimuthal step size of 0.25 deg. AMR was not used.

RCAS

Rotorcraft Comprehensive Analysis System (RCAS) (Refs. 19, 20) is a comprehensive analysis developed by the U.S. Army to provide statelof-the-art rotorcraft modeling and analysis technology for Government, industry, and academia. It is a multi-disciplinary software system capable of detailed modeling a wide range of rotorcraft configurations operating in hover, forward flight, and maneuvering flight to predict performance, loads, vibration, flight dynamics, and aeroelastic stability.

The ERATO rotor blade is modeled in RCAS using 18 nonlinear beam elements and 28 aerodynamic segments. As mentioned, both HOST and RCAS use the same airfoil tables generated by the U.S. Army. The rotor hub was modeled as fully articulated with pitch bearing and flap and lag hinges. The elastomeric lag damper of the ERATO rotor was modeled with equivalent hinge stiffness and damping values at the lag hinge. A 5.0 deg (72 steps per rotor revolution) azimuthal step size was used for the structural dynamic calculations in RCAS. The RCAS standalone analysis was conducted using nonuniform inflow with prescribed wake geometry and unsteady aerodynamics based on classical quasi-steady Theodorsen theory (Ref. 30).

CFD/CA coupled analysis

The CFD/CA coupling procedure used the standard partitioned loose or "delta" coupling approach (Ref. 1). At each coupling iteration the aerodynamic loads calculated by CFD are passed to CA. After trimming with the CFD airloads, CA computes the blade deflections and passes them back to CFD. This sequence is repeated until the airloads, deflections, and control angles converge. The trim parameters used in the predictions are the same as those from the test, a four degree-of-freedom trim. The trim targets are the specified rotor lift, rotor propulsive force and zero first harmonic flapping.

Both elsA and Helios CFD codes use overlapping grids consisting of structured curvilinear near-body grids rotating in a Cartesian background grid. All the CFD simulations considered in this work are assumed to be fully turbulent (i.e. no laminar-to-turbulent transition effects are modeled). The

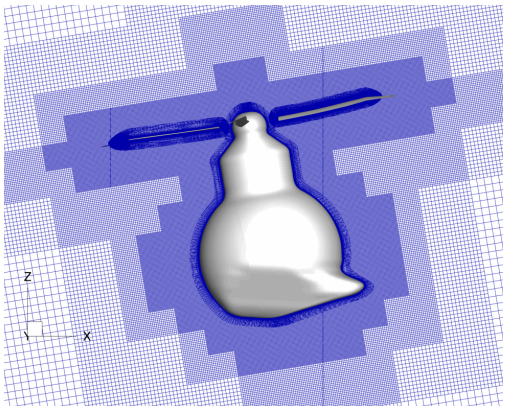

(a) elsA mesh.

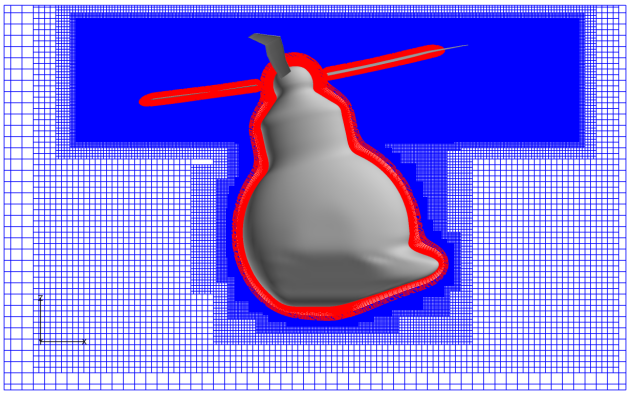

(b) Helios mesh.

Figure 2: Overset meshes used for the CFD analyses.

computational grids model the ERATO rotor blade geometry and test stand, but do not include a hub or the wind tunnel walls.

The size of the elsA grid shown in Figure 2.a is approximately 32.7M points: 5.5M points for blade body-fitted grids, 1M points for test stand, and 26.2M points for Octree background grid. The minimal grid size of the background mesh is approximately 9% of the main chord (0.14 m).

For Helios, shown in Figure 2.b, fully structured overset solver OVERFLOW was used for the ERATO blades. Each blade grid has approximately 13M nodes and the stand grid has approximately 1.6M nodes. In the off-body, 8 levels of grid are used with fixed refinement regions around the blade and test stand with a total of 757M nodes. For these regions, the finest grid spacing is approximately 6% of the tip chord.

In the HOST and elsA/HOST analyses, the blade is represented by the first eight eigenmodes and the blade periodic response was calculated with up to eight harmonics. For the RCAS and Helios/RCAS analyses, full finite element representation of the blade is maintained throughout the dynamic analysis and no harmonic truncation is used. Neither comprehensive analysis included blade structural damping, test stand dynamics, or drive train dynamics. Previous study showed that test stand and drivetrain dynamics for this test apparatus did not appear to play a significant role for rotor loads correlation (Ref. 5).

NUMERICAL ANALYSIS

In this work the double-swept ERATO rotor is studied under a high-advance-ratio condition. The ERATO rotor is a four-bladed fully articulated rotor, with a radius of 2.1 m and solidity, σ, of 0.085. The ERATO rotor blades have an aeroacoustically optimized design conceived by the DLR and ONERA in the 90s (Refs. 9, 10, 31, 32). One of the particularities of the blade is that it has a double-swept as shown in Figure 3. The linear twist rate is -10 deg/R. The blade is equipped with airfoils from OA family. The OA312 airfoil is used up 70% of the maximum radius. Then the airfoil transitions to OA409 at 90% and to OA407 at the blade tip. A large set of flight conditions were studied in different experimental campaigns in 1998. The forward-flight tests (used as a reference in this paper) were carried out at ONERA's S1MA wind tunnel in the Modane-Avrieux center located in the French Alps, the hover tests were performed in Marignane by Eurocopter (currently Airbus-Helicopters) and the aero-acoustic campaign took place at the DNW wind tunnel in Netherlands.

Figure 3: Planform of the ERATO blade.

A high-advance-ratio experimental point was chosen on this study ($\mu = 0.423$, $M_{Tip} = 0.616$, $C_L/\sigma = 0.06265$ and $C_x/\sigma = 0.0091$). Four degrees of freedom (dof) trim was carried out with the rotor thrust, propulsive force and zero flapping ($\beta_{1c} = \beta_{1s} = 0$) as objectives and controlled by the commands of the collective pitch angle, cyclic pitch angles (θ_0, θ_{1c} and θ_{1s} respectively) and the shaft angle (α_s).

The remainder of this section highlights two different aspects of the studied analysis. First, the capabilities of the proposed numerical tools are validated for the studied complex ERATO rotor emphasizing the difference between the rapid and the high-fidelity coupling tools. This study is carried out through a trim and power analysis and an airloads study at the specific sections of the blade where the experimental data is available. Second, a deeper study on the physical aspects of the high-advance-ratio flight is presented based sorely on the elsA/HOST computations.

Trim and power analysis

The converged values for trim commands and the rotor power are shown in Table 1. All the proposed methods provide a good prediction for the commands with a maximum relative

error with respect to the experimental trim of approximately 10% except for the θ_{1c} angle where the minimum error is provided by the elsA/HOST coupling (18%). Ortun et al. (Ref. 4) observed this phenomenon and highlighted that the test-stand has a non-negligible effect on the θ_{1c} angle. Thus, the important deviation ($> 54\%$) of the comprehensive tools (HOST and RCAS) with respect to the experimental results and the significant improvement of the high-fidelity couplings (Helios/RCAS and elsA/HOST) prediction is expected. This is due to the upwash (front side) and downwash (rear side) effect created by the test-stand and shown in Figure 4 which is not modelled by the comprehensive tools. About 1 deg error in the prediction of θ_{1c} is observed with the high-fidelity tools, however, a similar deviation was obtained for the 7A rotor analyses previously performed.

Table 1: Command and power values at convergence.

	θ_0 (deg)	θ_{1c} (deg)	θ_{1s} (deg)	α_s (deg)	P (kW)
Test	13.05	5.04	-10.06	-9.23	80.10
RCAS	11.49	2.31	-9.04	-10.17	84.64
HOST	12.03	1.87	-8.80	-9.56	91.16
Helios/RCAS	12.33	4.07	-9.88	-10.62	82.16
elsA/HOST	12.75	4.13	-9.53	-9.31	86.91

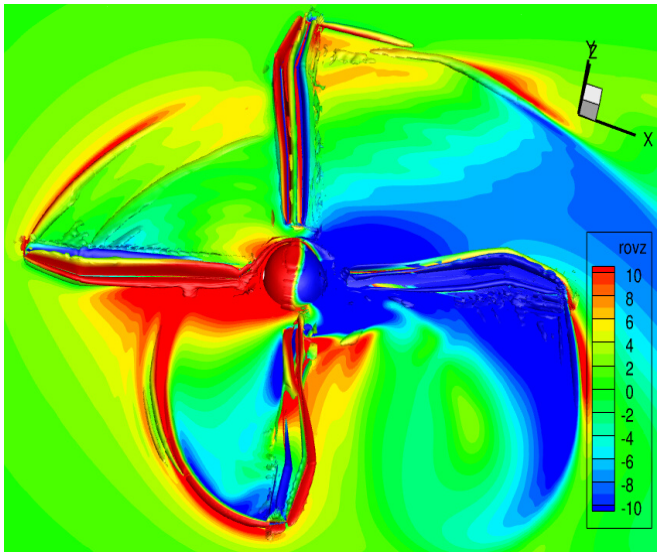

Figure 4: Upwash and downwash effect induced by the test-stand, elsA/HOST simulation.

As observed with the convergence of the commands, the power prediction is improved with the high-fidelity aerodynamics couplings. RCAS and Helios/RCAS provide a better agreement than HOST and elsA/HOST. This result is difficult to interpret due to several reasons: differences in trim control angles, differences in blade deformation or differences in the turbulence model and the numerical methods could impact the power prediction. Nevertheless, CFD codes tend to overestimate the power due to the fully turbulent modelling, used by Helios and elsA, which tends to overestimate the friction force and, thus, the blade profile drag power. Taking into account laminar-to-turbulent transition of the boundary layers could improve the predictions of the couplings with high-fidelity aerodynamics (Ref. 33).

Airloads

The section normal force (M^2Cn) and the section pitching moment (M^2Cm) are studied and compared to the experimental results at five different radial sections, corresponding to the 0.5, 0.75, 0.85, 0.925 and 0.975 relative-span (r/R), in order to validate the prediction of the comprehensive and high-fidelity tools. In the remainder of the article the color and style of these graphs are considered. Thus, the experimental results are plotted with a solid black line, the comprehensive analyses are shown with dashed lines while the high-fidelity results are solid lines, the results of the US Army are plotted in blue and the results of ONERA are green.

Figure 5 shows the M^2Cn load as a function of the azimuth at five radial positions. The normal lift coefficient (C_n) of the high-fidelity couplings is obtained by integrating the pressure coefficient (C_p) of the blade skin at the positions where the experimental Kulites are located. Between 90 deg and 120 deg azimuths a significant reduction of the M^2Cn is observed. This is an expected consequence of the rolling-moment compensation induced by the reduction of the command pitch angle of the advancing blade. While for the first radial position, the M^2Cn values remain positive, this effect is amplified through the span attaining an important negative M^2Cn value at the tip section (≈ -0.2). For all the radial positions, this negative trend and its amplitude are well represented. However, the comprehensive analyses are not capable of matching the azimuth of this lift-reduction. This is due to the transonic effect that creates a time-lag-effect which is missing on the 2D airfoil tables used by the comprehensive codes.

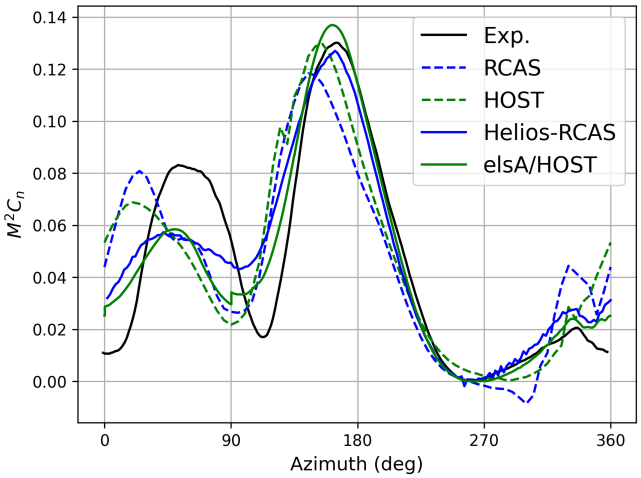

(a) Radial position: r/R= 0.5.

The high-fidelity CFD/CA couplings are capable of capturing this effect and matching the azimuthal position for the

minimum lift. Helios/RCAS seems to underpredict the amplitude of the lift-drop on the advancing blade while for the rest of the azimuths behaves similar to elsA/HOST. Between 270 deg and 300 deg, the M^2C_n presents some oscillations at the blade tip sections both in the experiment and in the high-fidelity analyses.

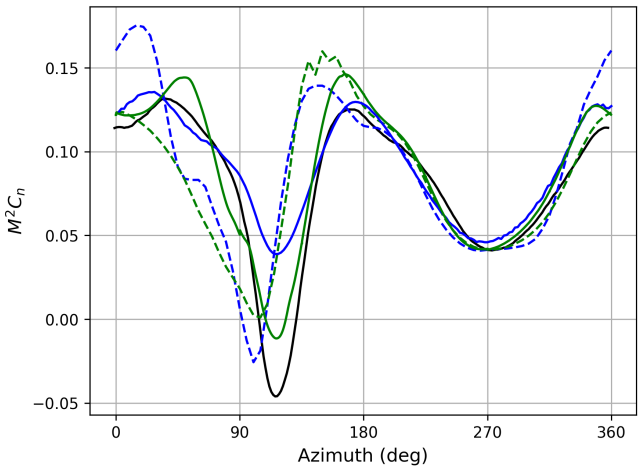

(b) Radial position: r/R= 0.75.

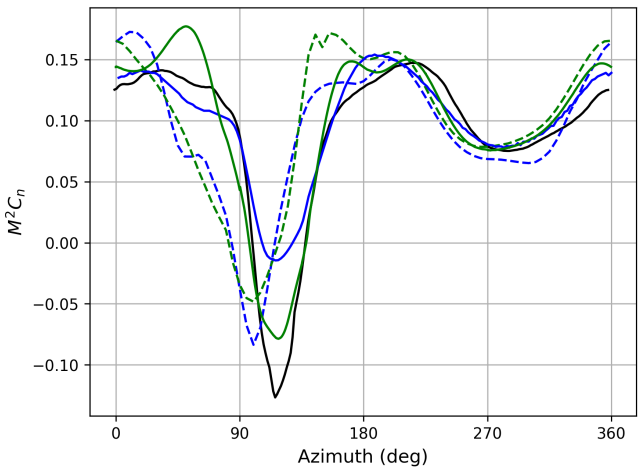

(c) Radial position: r/R= 0.85.

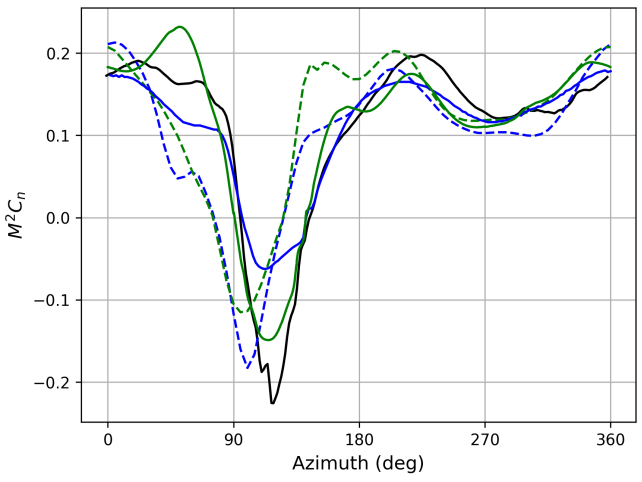

(d) Radial position: r/R= 0.925.

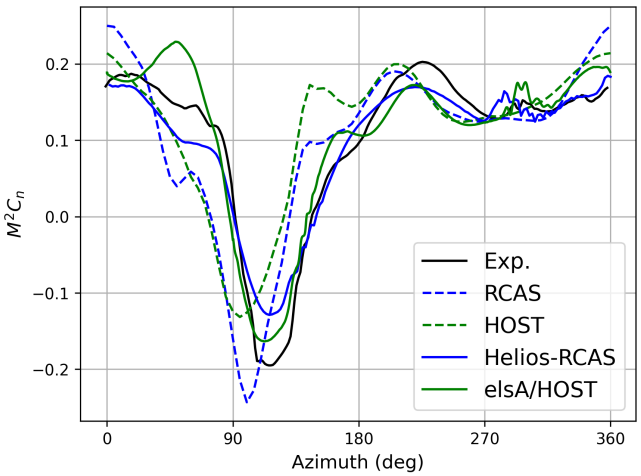

(e) Radial position: r/R= 0.975.

Figure 5: M^2C_n graphs at different radial positions.

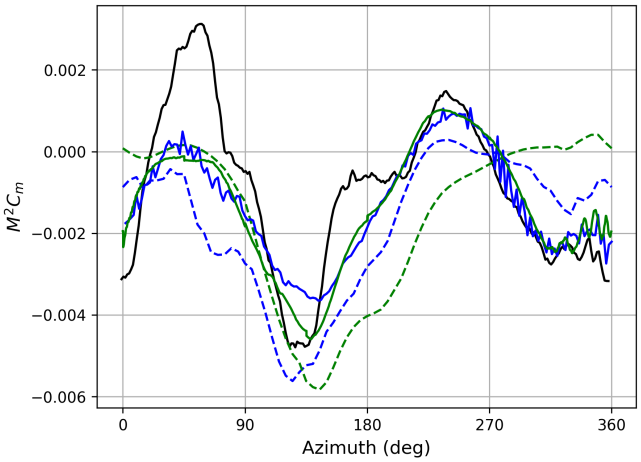

(a) Radial position: r/R= 0.5.

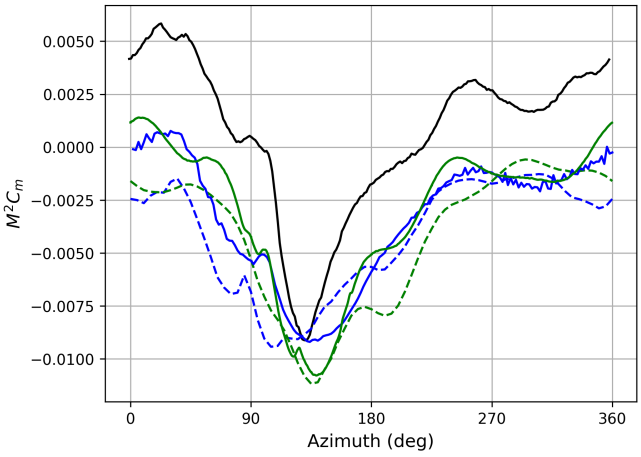

(b) Radial position: r/R= 0.75.

The M^2C_m moment is studied as a function of the azimuth in Figure 6 for the same radial positions as the M^2C_n. Similarly, the M^2C_m maximum and minimum values increase as the radial position approaches the tip of the blade.

At the most inboard sections (r/R< 0.75), both CA and

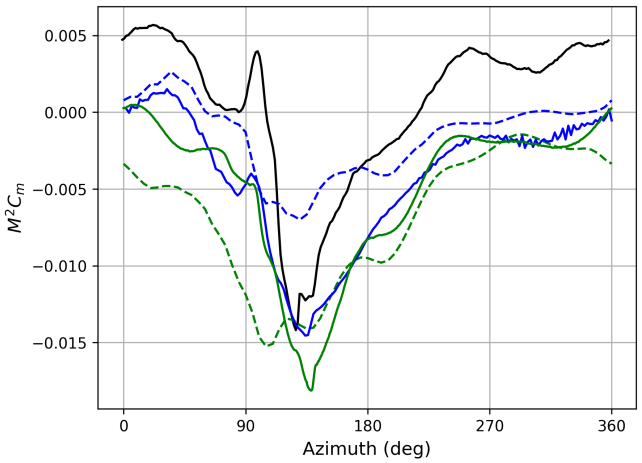

(c) Radial position: r/R= 0.85.

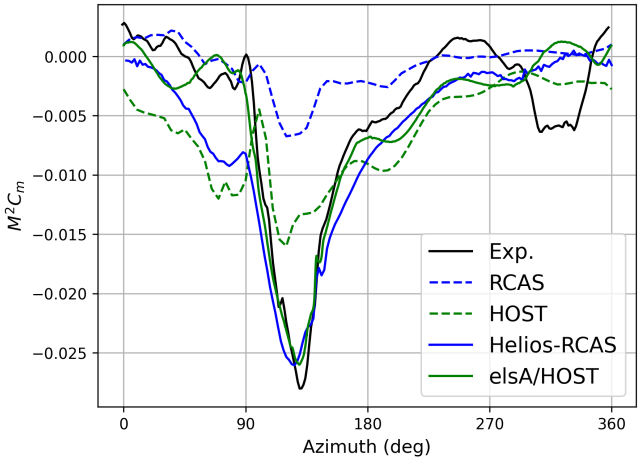

(d) Radial position: r/R= 0.925.

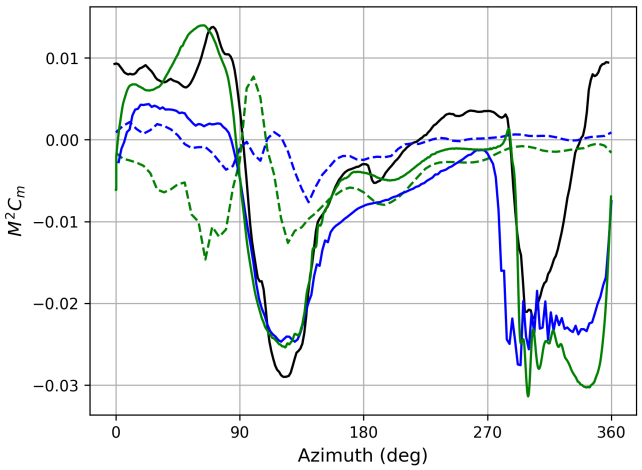

(e) Radial position: r/R= 0.975.

Figure 6: M^2C_m graphs at different radial positions.

CFD/CA simulations provide similar results. At the most outboard sections more discrepancies between the numerical results appear. HOST and RCAS underpredict the negative peak on the advancing blade close to the tip. On the retreating blade, the experiment shows a drop of the pitching moment between 270 deg and 300 deg located at 0.925 r/R and 0.975 r/R sections. This effect could be identified as a pitching-moment dynamic-stall. An interesting aspect of this behavior, is that no dynamic-stall is observed on the M^2C_n analyses at the same radial positions (Figures 5.d and 5.e). This shows that even if a pitching moment stall appears, the blade continues to provide lift. This non-conventional behavior could be a consequence of the unusual blade tip shape. The origins of this result will be discussed later in the paper. Generally, the high-fidelity CFD/CA coupling significantly improves the M^2C_m response, however, even if for most of the forms of the response are reproduced both by elsA/HOST and Helios/RCAS, the first radial positions M^2C_m show a shift towards an over-prediction of the negative average (Figures 6.a, 6.b and 6.c). In the two tip radial sections (Figures 6.d and 6.e), the response is properly captured both in terms of shift and magnitude. In the experiment, the radial extension of the pitching moment dynamic stall seems to be larger than the one predicted by the numerical analyses as the high-fidelity coupling does not reproduce the reduction of M^2C_m in the pitching-moment dynamic-stall region at 0.925 r/R (Figure 6.d). On the advancing blade side, both coupling methods improve the prediction of the negative pitching moment on the blade tip between 100 deg and 120 deg of azimuth, while CA tools tend to underestimate the strong amplitude variation.

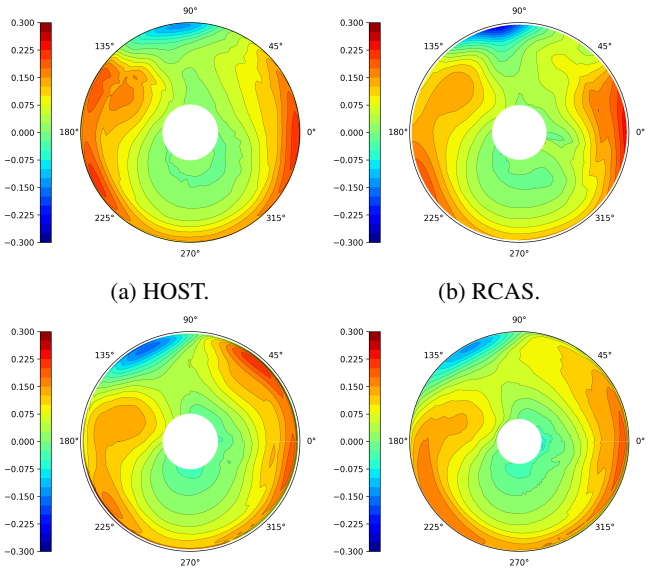

(a) HOST. (b) RCAS.

(c) elsA/HOST. (d) Helios/RCAS.

Figure 7: M^2C_n rotor map.

Figures 7 and 8 show respectively the M^2C_n and M^2C_m rotor map of the analytical analyses provided by the simulations without considering the Kulites integration. As discussed previously, the transonic effect induces a delay on the azimuthal position of the negative lift on the tip of the advancing blade. The CA tools predict the negative lift on the tip of the blade in the neighborhood of 90 deg. In terms of magnitude, RCAS seems to perform better than HOST which underestimates the minimum lift value. Similarly, CA tools seem to overestimate the positive lift regions at 180 deg and 0 deg while elsA/HOST

coupling seems to have an extended maximum lift region but with smaller magnitude. The M^2C_m rotor map shows larger variations with the high-fidelity CFD/CA analyses, specially at the blade tip. The advancing blade observes a negative moment on its tip between 90 deg and 120 deg as expected at high-speed forward-flight. This effect is slightly observed by the CA tools. Between 270 deg and 300 deg, where the dynamic stall appears, the high fidelity CFD/CA predict a positive moment on the blade root and a negative moment effect on the blade tip. The root moment is slightly captured by the CA tools.

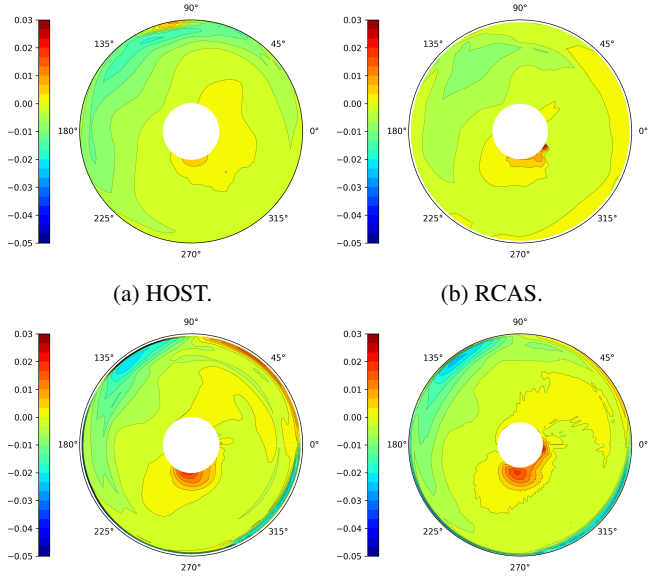

(a) HOST. (b) RCAS.

(c) elsA/HOST. (d) Helios/RCAS.

Figure 8: M^2C_m rotor map.

Wake analysis

Different authors in literature have identified a Blade-Vortex-Interaction (BVI) as a trigger of dynamic stall on the retreating blade side (Ref. 7), especially for an advance-ratio of 0.3. At higher advance-ratio and for non-conventional blade-shape, the role of the rotor wake in stall triggering is not clear. Furthermore, the advancing blade side is also a potential region of BVI that could impact the evolution of the airloads. Thus, this section aims to identify the interaction between the wakes and the blades on both the advancing and the retreating sides. This study is mostly carried out with the results obtained from the elsA/HOST coupling.

Figure 9.a shows the wake of the advancing blade at 90 deg. The iso-Q criterion is colored by the vertical velocity highlighting the rotation direction of the vortices (defined by the arrows). It is observed that the wake faints and changes its rotation direction due to the lift sign variation observed at the tip of the blade generating wakes that turn oppositely. Figure 9.b shows a BVI on the advancing blade at the tip of the blade. While the blade advances, the location of this interaction shifts towards inner positions. Downstream, the stream-

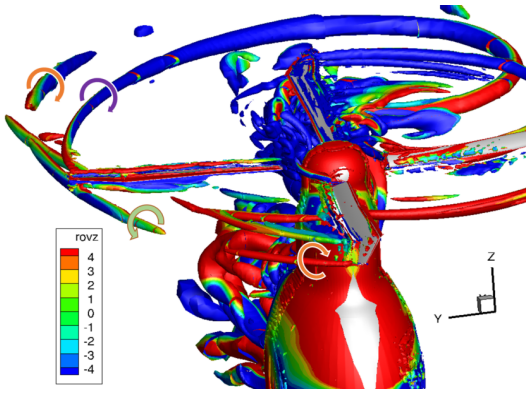

(a) Advancing blade vortex rotation, 90 deg, elsA/HOST.

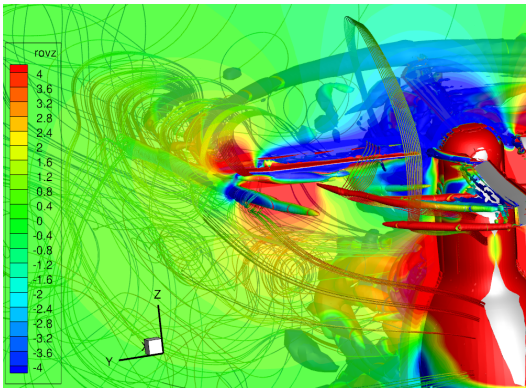

(b) Advancing blade, 90 deg, elsA/HOST.

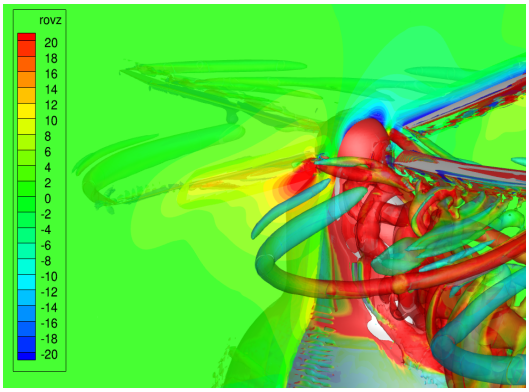

(c) Retreating blade, azimuth 270 deg, elsA/HOST.

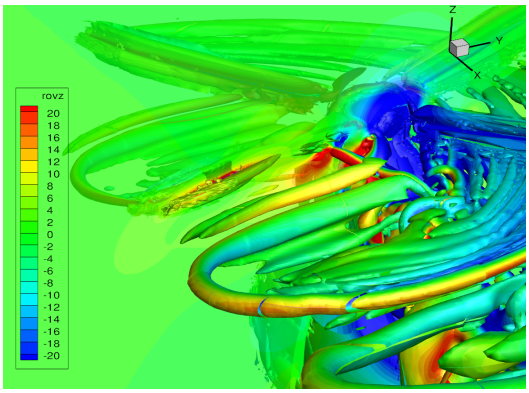

(d) Retreating blade, azimuth 300 deg, elsA/HOST.

Figure 9: Wake interaction analysis.

lines show that the previous wake interacts with the new tip-vortex and both of them interact in a complex manner.

Figures 9.c and 9.d depict the wake on the retreating blade side. These figures show that the tip of the blade does not interact with the previous wakes between 270 deg and 300 deg azimuth. Thus, it could be concluded that the pitching-moment-dynamic-stall is most probably not induced by a BVI. The velocity field at the LE of the blade remains unchanged and is not impacted by the wake. The tip vortex seems to be generated perpendicularly to the blade for most of the cases, however, at the 300 deg azimuthal position the wake seems to be more aligned with the blade axis.

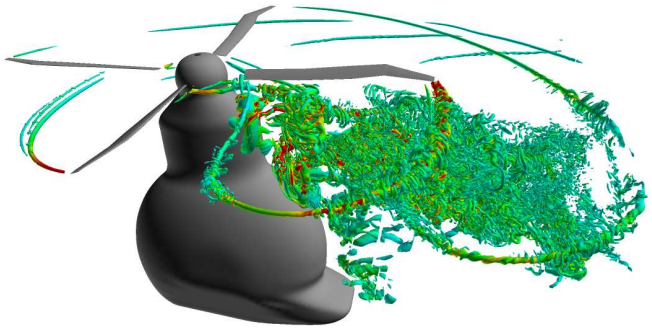

(a) Iso-Q criterion Helios/RCAS, retreating blade at 270 deg.

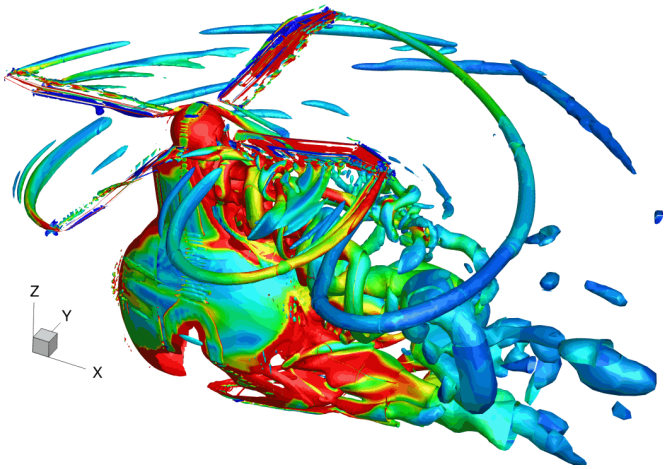

(b) Iso-Q criterion elsA/HOST, retreating blade at 270 deg.

Figure 10: Iso-Q criterion, wake representation.

Figure10 shows the isoQ-criterion colored by the vorticity magnitude in order to observe the wake of all the blades and the test stand when the retreating blade is located at 270 deg of azimuth. As discussed previously, a BVI is observed on the advancing blade due to the proximity of the wakes generated at the previous blade both at the tip and the position of the swept inflection. However, the impact of this interaction seems small. The retreating blade does not present a BVI due to the high-advance-ratio value.

Both Helios/RCAS and elsA/HOST provide similar wake results. The wake structures with Helios seem to be more discretized due to a finer mesh and a DDS. The trajectory of the wakes and the effect of wake fainting on the advancing blade is also present at similar locations.

Chord-wise aerodynamics of the blade tip

In order to validate the chord-wise prediction of the loads computed by the CFD/CA couplings and to study the behavior of the blade tip, Figure 12 shows the pressure coefficient C_p with respect to the normalized chord-wise coordinate (x/c) where 0 corresponds to the leading-edge (LE) and 1 to the trailing-edge (TE).

Six azimuthal positions (0.4 deg, 90 deg, 120 deg, 180 deg, 270 deg and 300 deg) where the experimental data was available are studied using the high-fidelity CFD/CA results for the two tip sections (0.925 and 0.975 r/R). Overall, the numerical predictions are capable of accurately capturing the various phenomena that take place over the blade (i.e. shocks magnitude and position, stall).

Figures 12.a and 12.d show that the blade at 0.4 deg is operating nominally with the maximum absolute values of C_p both for the pressure and section sides (maximum lift condition) located close to the LE of the blade, the flow remains attached through all the profile.

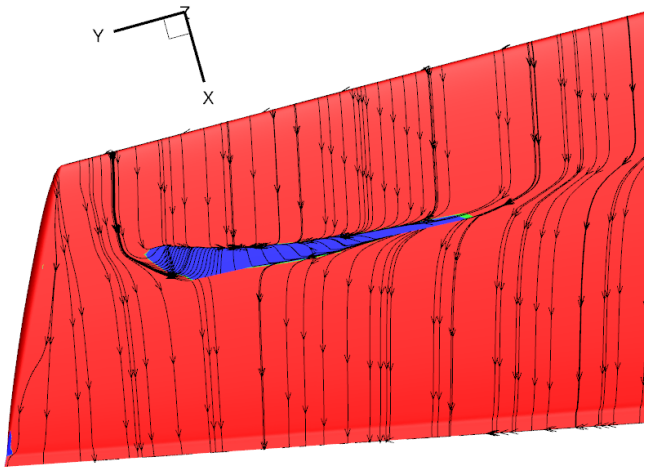

Figure 11: Pressure side at 120 deg azimuth.

Regarding the lift-drop that occurs between 90 deg and 120 deg, the blade presents a sonic shock at the suction side (0.2 x/c) close to the LE depicted in Figures 12.b and 12.e. At the pressure side close to the LE a reduction of the friction coefficient is observed leading to a pre-bubble state with a large suction peak. The position of these effects induces an additional pitching moment to the blade. While the blade advances on its azimuthal position, at 120 deg, the sonic shock of the suction side is diffused which induces a large suction effect. Figure 11 shows the pressure side of the advancing blade at 120 deg. The streamlines and the friction vector show that a recircula-

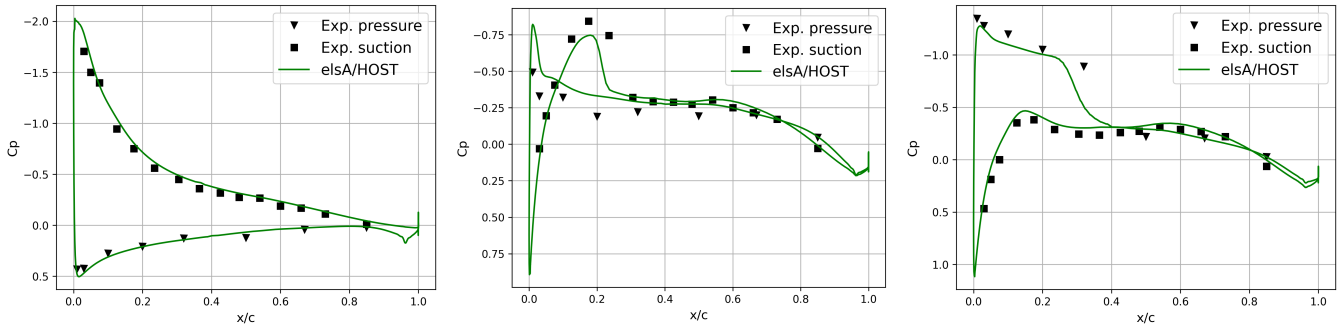

(a) Azimuth 0.4 deg, 0.925 r/R.

(b) Azimuth 90 deg, 0.925 r/R.

(c) Azimuth 120 deg, 0.925 r/R.

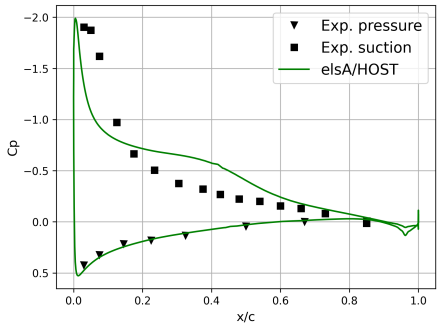

(d) Azimuth 0.4 deg, 0.975 r/R.

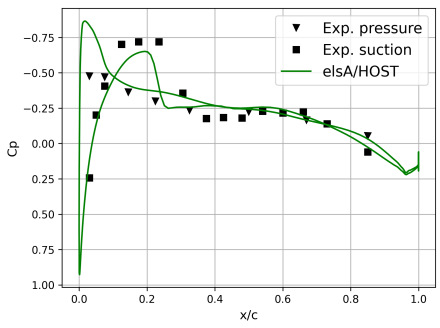

(e) Azimuth 90 deg, 0.975 r/R.

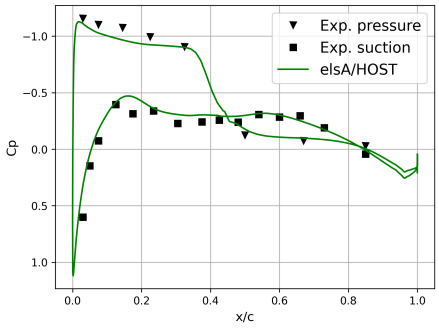

(f) Azimuth 120 deg, 0.975 r/R.

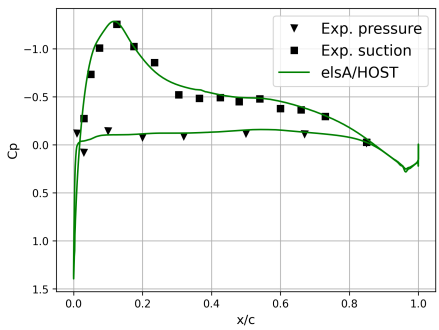

(g) Azimuth 180 deg, 0.925 r/R.

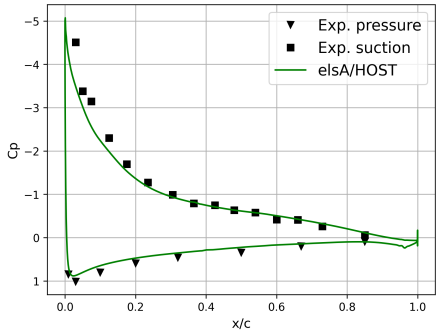

(h) Azimuth 270 deg, 0.925 r/R.

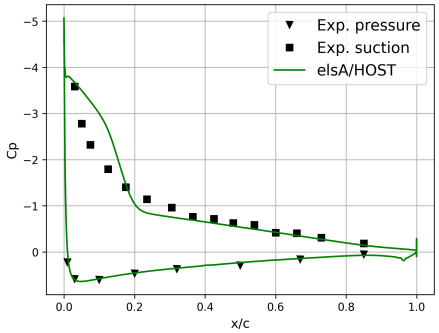

(i) Azimuth 300 deg, 0.925 r/R.

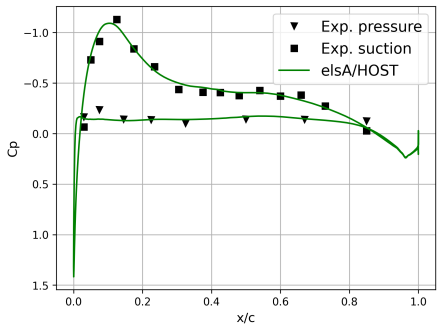

(j) Azimuth 180 deg, 0.975 r/R.

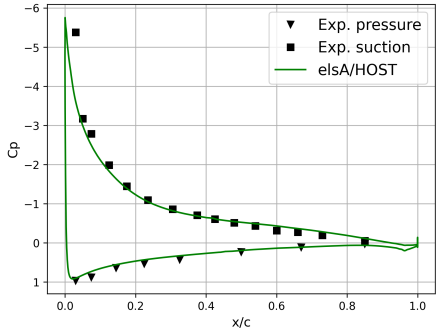

(k) Azimuth 270 deg, 0.975 r/R.

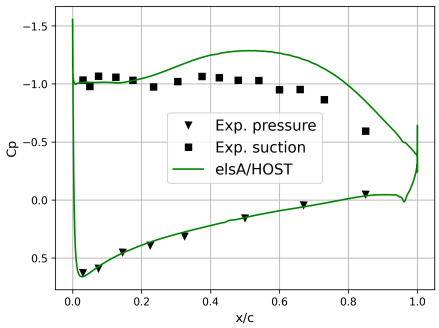

(l) Azimuth 300 deg, 0.975 r/R.

Figure 12: C_p distribution at different radial locations.

tion bubble is present. This recirculation bubble is responsible of the large Cp plateau observed in Figures 12.c and 12.f.

As shown in Figures 12.g and 12.j, at 180 deg, the blade behaves nominally as a profile under low angle of attack.

Figures 12.h and 12.k present the rotor before the appearance of the dynamic stall. At 270 deg the blade responds like a profile at low velocity and high angle of attack with an attached boundary layer.

At 300 deg azimuth, Figures 12.i and 12.l, a pitching-moment-dynamic-stall behavior is present without any lift-stall. A suc-

tion effect appears in the TE due to a boundary-layer detachment through all the suction side while the pressure side behaves nominally. This interesting behavior is due to a LE vortex which is classical for propellers with large swept and delta wings (Ref. 34). Figure 13 shows the streamlines generated on the blade tip colored by the vertical velocity and the blade surface colored by the total pressure. The region in blue on the blade surface represents a loss of total pressure and indicates the position of the tip vortex. This effect creates a suction region with large magnitude close to the LE. The lack of lift-stall is probably due to the lifting effect of this vortex. When the vortex detaches from the leading edge, it induces the stall of the moment studied previously. The tip-vortex and the LE vortex finally create a common vortex whose initial direction has a larger tangential component with respect to the classical perpendicular tip-vortex generation.

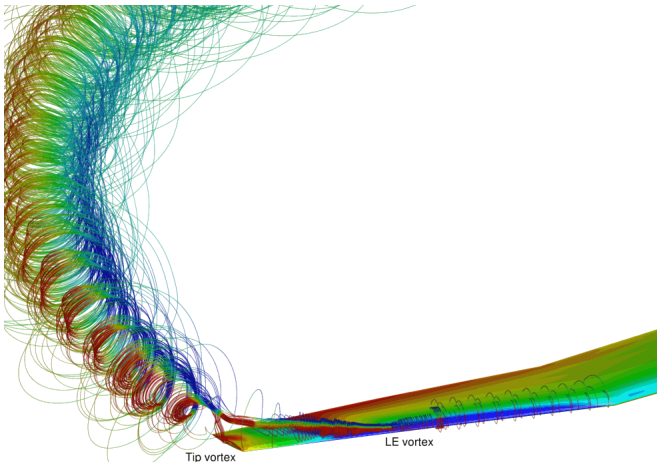

Figure 13: LE vortex generation.

SUMMARY AND CONCLUSIONS

This article presents the aerodynamic loads analysis of the double-swept ERATO rotor under high-advance-ratio level-flight condition. This work was developed in the framework of the United States/France Project Agreement on Rotatory Wing Aeromechanics and Human Factors Integration Research. Different CA and CFD/CA tools are presented and compared (RCAS, Helios/RCAS, HOST and elsA/HOST). The trim and airloads are compared to the experimental data. An special attention is taken to the wake interactions and the in-chord behavior of the blade aerodynamics. From this study, the following conclusions are obtained:

- Comprehensive analyses tend to underpredict blade pitch angles. Coupled analyses, which include the test-stand modeling, increase blade pitch angles and improve overall correlation. Especially, improvement of lateral cyclic angle correlation is notable.

- The rotor blade aerodynamic environment at high speed is characterized by compressibility, and negative lift and large aerodynamic pitching moment on the advancing side. The experimental data of the ERATO rotor show that a pitching-moment dynamic-stall is observed on the retreating side. Despite the pitching-moment dynamic-stall, the lift does not stall.

- For the normal force comparison, the standalone comprehensive analyses show reasonably good correlation on magnitude, but the phase correlation is poor. This is due to the limitations of the 2D airfoil tables. The coupled analyses significantly improve the phase of the negative lift and waveform in the first quadrant. A large aerodynamic pitching moment on the advancing side and pitching-moment dynamic-stall on the retreating side are also better captured by the coupled analyses than the comprehensive analyses based on lifting-line aerodynamics.

- On the advancing blade side, the high-fidelity simulations show that the variations of the normal force from positive to negative induces a change of the rotation direction of the tip vortex.

- The high-advance-ratio condition implies that the retreating blade does not interact with the wake of the previous blades.

- The high-fidelity couplings are capable of capturing the pressure distribution on the chordwise direction accurately.

- The amplitude of the negative pitching moment observed on the advancing blade is increased due to the existence of a sonic shock on the suction side of the blade at $0.2x/c$ and a suction effect close to the leading edge on the pressure side. Once the minimum value is reached a recirculation bubble appears on the pressure side and the sonic shock on the suction side is diffused.

- The high-fidelity coupling simulations show that, on the retreating side, a leading edge vortex appears and then mixes with the tip vortex modifying its initial direction. This leading edge vortex induces a pitching-moment stall but due to its suction effect, it allows providing lift, which explains the experimental observations.

REFERENCES

1. Mark Potsdam, Hyeonsoo Yeo, and Wayne Johnson. Rotor airloads prediction using loose aerodynamic/structural coupling. *Journal of Aircraft*, 43(3):732–742, 2006.

2. Hyeonsoo Yeo and Mark Potsdam. Rotor structural loads analysis using coupled computational fluid dynamics/computational structural dynamics. *Journal of Aircraft*, 53(1):87–105, 2016.

3. François Richez, Rohit Jain, Marilyn Smith, Amanda Grubb, and Camille Castells. Validation and analysis

of aeroelastic simulations of the uh-60a rotor from pre- to post-stall flight conditions. In *76th Annual Forum & Technology Display (Vertical Flight Society)*, 2020.

4. Biel Ortun, Mark Potsdam, Hyeonsoo Yeo, and Khiem Van Truong. Rotor loads prediction on the onera 7a rotor using loose fluid/structure coupling. *Journal of the American Helicopter Society*, 62(3):1–13, 2017.

5. Hyeonsoo Yeo, Mark Potsdam, Biel Ortun, and Khiem Van Truong. High-fidelity structural loads analysis of the onera 7a rotor. *Journal of Aircraft*, 54(5):1825–1839, 2017.

6. François Richez. Analysis of dynamic stall mechanisms in helicopter rotor environment. *Journal of the American Helicopter Society*, 63(2):1–11, 2018.

7. Camille Castells, François Richez, and Michel Costes. A numerical analysis of the dynamic stall mechanisms on a helicopter rotor from light to deep stall. *Journal of the American Helicopter Society*, 65(3):1–17, 2020.

8. Biel Ortun, Didier Petot, Khiem-Van Truong, and Roger Ohayon. Towards a new generation of rotorcraft comprehensive analysis; coupling with csm and cfd. 2008.

9. Philippe Beaumier, Berend G van Der Wall, Kurt Pengel, Christoph Kessler, Marc Gervais, Yves Delrieux, Jean-François Hirsch, and Pascal Crozier. From ERATO basic research to the blue edgetm Blue Edge^{TM} rotor blade: an example of virtual engineering? In *Rotorcraft Virtual Engineering Conference*, 2016.

10. Y Delrieux, J Prieur, M Costes, P Gardarein, P Beaumier, H Mercier des Rochettes, P Leconte, P Crozier, WR Splettstoesser, B Van der Wall, et al. The onera-dlr aeroacoustic rotor optimisation programme erato: methodology and achievements. In *American Helicopter Society Aerodynamics, Acoustics and Test and Evaluation Technical Specialists Meeting, San Francisco*, 2002.

11. Felix Frey, Jakob Thiemeier, Constantin Öhrle, Manuel Keßler, and Ewald Krämer. Aerodynamic interactions on airbus helicopters' compound helicopter racer in cruise flight. *Journal of the American Helicopter Society*, 65(4):1–14, 2020.

12. Boisard Ronan. Time efficient methodology for the evaluation of aerodynamics and flight mechanics of the racer compound helicopter in hover under cross wind conditions. In *VFS 68-Forum 68-The Vertical Flight Society*, 2022.

13. Constantin Öhrle, Felix Frey, Jakob Thiemeier, Manuel Keßler, and Ewald Kräamer. Coupled and trimmed aerodynamic and aeroacoustic simulations for airbus helicopters' compound helicopter racer. *Journal of the American Helicopter Society*, 64(3):1–14, 2019.

14. Jinggen Zhao, Mikel Brigley, Ramin Modarres, and William A Welsh. S-97 raider rotor vibratory loads analysis using cfd-csd. In *AIAA SciTech 2019 Forum*, page 0860, 2019.

15. Yeo Hyeonsoo, Balmaseda Aguirre Mikel, Jayaraman Buvana, Richez François, and Ortun Biel. High-fidelity structural loads analysis of the double-swept erato rotor. In *50th European Rotorcraft Forum, Marseille, France*, September 10-12,2024.

16. L Cambier, M Gazaix, S Heib, S Plot, M Poinot, JP Veuillot, JF Boussuge, and M Montagnac. An overview of the multi-purpose elsa flow solver. *Aerospace Lab*, (2):p–1, 2011.

17. Bernard Benoit, Konstantin Kampa, W von Grunhagen, Pierre-Marie Basset, and Bernard Gimonet. Host, a general helicopter simulation tool for germany and france. In *Annual Forum Proceedings-American Helicopter Society*, volume 56, pages 1110–1131. American Helicopter Society, INC, 2000.

18. Andrew M Wissink, Dylan Jude, Buvaneswari Jayaraman, Beatrice Roget, Vinod K Lakshminarayan, Jayanarayanan Sitaraman, Andrew C Bauer, James R Forsythe, and Robert D Trigg. New capabilities in CREATE^{TM}-av helios version 11. In *AIAA Scitech 2021 Forum*, page 0235, 2021.

19. Hossein Saberi, Matthew Hasbun, J Hong, Hyeonsoo Yeo, and Robert A Ormiston. Overview of rcas capabilities, validations, and rotorcraft applications. In *American Helicopter Society 71st Annual Forum, Virginia Beach, VA*, 2015.

20. Matthew Hasbun, Hossein Saberi, and Hyeonsoo Yeo. Overview of rcas capabilities and validations for rotorcraft and evtol applications. In *Vertical Flight Society 80th Annual Forum & Technology Display, Montreal, Canada*, 2024.

21. Christophe Benoit, Stéphanie Péron, and Sâm Landier. Cassiopee: a cfd pre-and post-processing tool. *Aerospace Science and Technology*, 45:272–283, 2015.

22. J. C. Kok. Resolving the dependence on freestream values for the k-ω turbulence model. *AIAA Journal*, 38:1292–1295, July 2000.

23. Manikandan Ramasamy, Rohit Jain, and Thomas R Norman. Data-driven analysis of cycle-to-cycle variations, scatter, and furcation in the uh-60a wind tunnel rotor airloads measurements. *Journal of the American Helicopter Society*, 67(4):1–21, 2022.

24. X Zheng, C Liao, C Liu, CH Sung, and TT Huang. Multigrid computation of incompressible flows using two-equation turbulence models: Part i—numerical method. 1997.

25. RH Nichols and PG Buning. Overfow user's manual, version 2.2. *NASA Langley Research Center, Hampton, VA*, 2010.

26. Robert T Biedron, Jan-Reneé Carlson, Joseph M Derlaga, Peter A Gnoffo, Dana P Hammond, Kevin E Jacobson, William T Jones, Bil Kleb, Elizabeth M Lee-Rausch, Eric J Nielsen, et al. Fun3d manual: 13.7. Technical report, 2020.

27. David R McDaniel, Todd Tuckey, and Scott A Morton. The hpcmp CREATE^{TM}-av kestrel computational environment and its relation to nasa's cfd vision 2030. In *55th AIAA Aerospace Sciences Meeting*, page 0813, 2017.

28. Jayanarayanan Sitaraman, Vinod K Lakshminarayan, Beatrice Roget, and Andrew M Wissink. Progress in strand mesh generation and domain connectivity for dual-mesh cfd simulations. In *55th AIAA Aerospace Sciences Meeting*, page 0288, 2017.

29. Wayne Johnson. Technology drivers in the development of camrad ii. In *American helicopter society aeromechanics specialists conference, San Francisco, California*, pages 3–1, 1994.

30. Theodore Theodorsen. General theory of aerodynamic instability and the mechanism of flutter. Technical report, 1979.

31. Jean Prieur and Wolf R Splettstoesser. Erato-an onera-dlr cooperative programme on aeroacoustic rotor optimization. 1999.

32. WR Splettstoesser, BG van der Wall, B Junker, K-J Schultz, P Beaumier, Y Delrieux, P Leconte, and P Crozier. The erato programme: wind tunnel test results and proof of design for an aeroacoustically optimised rotor. 1999.

33. Rohit Jain. Computational fluid dynamics transition models validation for rotors in unsteady flow conditions. *Journal of Aircraft*, 59(4):875–895, 2022.

34. Ye-Bonne Koyama. *Characterisation and aerodynamic impact of leading-edge vortices on propeller blades*. PhD thesis, Université Paris Saclay (COmUE), 2018.